The Madden–Julian Oscillation in an Idealized General Circulation Model

NGAR-CHEUNG LAU AND ISAAC M. HELD

Geophysical Fluid Dynamics Laboratory/NOAA, Princeton, New Jersey

J. DAVID NEELIN*

Program in Atmospheric and Oceanic Sciences, Princeton University, Princeton, New Jersey

ABSTRACT

The structure of the intraseasonal oscillations in the tropics of an idealized general circulation model with a zonally symmetric climate is described. Space–time spectra show a peak in zonal winds and velocity potential at the equator in zonal wavenumbers 1 and 2, corresponding to eastward-propagating power at phase speeds of ≈ 18 m s^{-1}. This speed is significantly greater than that of the observed oscillation but comparable to that obtained in similar models by Hayashi and Sumi and Swinbank et al. The corresponding eastward-propagating power in the precipitation spectrum is concentrated in wavenumbers 2–5. A composite procedure is used to describe the three-dimensional structure of the model's oscillation. The oscillation is characterized by circulation cells oriented along the equatorial zonal plane, with enhanced precipitation in the region of rising motion. Zonal wind changes tend to be positively correlated with geopotential height changes at the same level. Positive perturbations in the water vapor mixing ratio, evaporation, and lower tropospheric horizontal moisture convergence all exhibit distinct eastward displacements from the center of convection.

Two different linear models are used to interpret the GCM results. The response to the GCM's composited diabatic heating field is first computed using a linear primitive equation model on the sphere. This linear model requires strong damping above the heated region, as well as near the surface, to produce a pattern in rough agreement with the GCM. A simple Kelvin wave-CISK model, in which the vertical structure of the heating is taken from the composite, is then shown to be capable of reproducing the phase speed simulated in the GCM.

1. Introduction

Analysis of the dynamics of the 40–50 day tropical oscillation first detected by Madden and Julian (1971, 1972) has recently been aided by studies of the analog of this oscillation in general circulation models (GCMs). Lau and Lau (1986) have described some of the characteristics of the tropical intraseasonal oscillations in the GCM developed by the climate dynamics group at the Geophysical Fluid Dynamics Laboratory (GFDL). This model has realistic land–sea distribution and orography and a seasonal cycle of insolation but relatively low resolution (rhomboidal truncation at wavenumber 15). The model-generated oscillations resemble those observed in a number of respects. They are associated with eastward-traveling circulation cells oriented along the equatorial plane, with perturbations

in the zonal wind, geopotential and horizontal divergence at the tropopause opposite in phase to the corresponding perturbations near the ground. The passage of these circulation cells modulates the precipitation in the monsoon regions over the Indian and western Pacific Oceans, with the precipitation exhibiting northward propagation within the summer monsoon region. The scale of the pressure and wind patterns is larger than that of the precipitation changes, the former being dominated by zonal wavenumbers 1 and 2. The oscillations are present throughout the year, with slight displacements about the equator from winter to summer. The dominant periods of the wavenumber 1 component of the model's disturbances are 25–40 days, corresponding to phase speeds (≈ 10–18 m s^{-1}) that are considerably faster than the observed phase speed. Hayashi and Golder's (1986) comparison of this model with a higher resolution model with essentially identical physics shows that the higher resolution model exhibits a stronger signal at lower frequencies. Their results also suggest that the higher resolution model has two distinct spectral peaks corresponding to periods of ≈ 40 days and ≈ 25 days for wavenumber 1. If one accepts the assertion that the essential dynamics of the oscillation has been captured in these models, one must also agree that mechanisms such as feedbacks with cloud cover

* Present affiliation: Department of Atmospheric Sciences, University of California, Los Angeles, CA.

Corresponding author address: Dr. Ngar-Cheung Lau, Geophysical Fluid Dynamics Laboratory, Princeton University, P.O. Box 308, Princeton, NJ 08542.

and ocean temperature are not essential to the existence of the oscillation, since these are not included in the GCMs.

The observed convective activity associated with the tropical oscillations is known to be largely confined to the Indian Ocean and the western Pacific Ocean (e.g., Knutson and Weickmann 1987). Such geographical dependence of the precipitation signal is also present in GCM runs with realistic land–sea contrasts and orography (e.g., Lau and Lau 1986, Fig. 11c). However, Hayashi and Sumi (1986) have detected intraseasonal oscillations in an idealized GCM with a zonally symmetric climate. Their model has a flat lower boundary with a specified zonally symmetric temperature at the boundary. Their study suggests that zonal inhomogeneities in the climatological tropical convection and orography are not essential to the existence of the Madden–Julian oscillation. This result has been confirmed in a model with similar fixed-temperature boundary conditions by Swinbank et al. (1988), who were able to change the frequency of the oscillation by increasing the strength of the latent heating in their model. Neelin et al. (1987, hereafter referred to as NHC) also found low-frequency, eastward-propagating tropical oscillations in two GCMs with zonally symmetric climates, one with zonally uniform prescribed surface temperatures and another with a zero-heat capacity ("swamp") lower boundary condition. By modifying the lower boundary condition so as to remove the evaporation anomalies associated with the surface wind fluctuations, they were able to reduce the amplitude of the oscillation in the fixed surface temperature model (but not in the swamp model).

Such idealized GCMs with zonally symmetric climates appear to provide a good laboratory for further study of this oscillation. The zonal homogeneity simplifies the analysis and allows one to define the structure of the oscillations with some precision. In the present paper, we describe the spatial and temporal structure of tropical oscillations occurring in one of the idealized models discussed by NHC. We consider only the model with fixed ocean temperatures, as it is more directly relevant to the (mostly) ocean-covered tropics than is the swamp model.

The global spectral model studied has the same resolution as the model with realistic boundary conditions analyzed by Lau and Lau, i.e., rhomboidal truncation at wavenumber 15, and nine σ-levels in the vertical. The lower boundary is a flat, saturated surface with temperatures fixed at values that are a function of latitude only. These temperatures are symmetric about the equator and are set equal to those predicted by the companion swamp model. Annual mean solar input is prescribed at the upper boundary, clouds are prescribed as a function of latitude only, and surface albedos are fixed at 0.1 everywhere. The clouds are also symmetric about the equator. Convection is modeled by the moist convective adjustment parameterization

scheme described by Manabe et al. (1965). The GCM has been integrated for 1400 days after discarding a spinup of several hundred days.

The resulting climate has a single maximum in tropical rainfall at the equator. This is quite unlike the idealized GCMs of Hayashi and Sumi (1986) and Swinbank et al. (1988), in which there is a split ITCZ and an equatorial dry zone. Our tentative explanation for this difference can be found in appendix A.

In this paper, particular emphasis is placed on the detailed vertical structure of the oscillation and also on those parameters of importance for studying the interaction between the flow field and moist convection, such as the water vapor content, evaporation rate, and the heating due to the model's convective parameterization. We begin by describing some space–time spectra that emphasize the different scales of the horizontal flow field and the precipitation anomalies. Most of the paper is then devoted to the results of a composite analysis focused on the larger scales. To examine the relationship between the flow field and the diabatic heating, we also use a diagnostic linear wave model forced by the traveling heating field obtained from the composite analysis. Finally, we present a simple wave-CISK model that mimics some aspects of the GCM's oscillation.

2. Spectra

Figure 1 shows the frequency spectra of the zonal velocity at (a) 205 and (b) 940 mb for zonal wavenumbers 1–5, averaged over the two grid points at 2.25°S and 2.25°N. The simulation is sampled once a day. The total 1400-day time series is split into two equal parts, and the spectra of the two parts are displayed separately to provide some indication of statistical significance. The bandwidth is 0.011 cycles per day, and a half-cosine weighting is used on the first and last 10% of each time series. Figure 2 contains analogous plots for the equatorial (a) velocity potential at 205 mb and (b) precipitation.

We interpret the peak in the velocity potential and zonal velocity spectra for eastward-propagating wavenumber 1 centered at a period of 24 days as the model's analog of the Madden–Julian oscillation. The period is consistent with that found by Lau and Lau and in the idealized GCMs of Hayashi and Sumi and Swinbank et al., but is significantly shorter than the observed period. The differences between the two halves of the integration warn us not to take details of the shape of the peak seriously. The corresponding peak in wavenumber 2 is centered at about 12 days, which corresponds to roughly the same phase speed, ≈ 18 m s^{-1}, as the wavenumber 1 perturbation. A smaller and less well defined peak at a similar phase speed is also evident in wavenumber 3 in the velocity potential. These results argue against those theories that provide a mechanism for frequency selection rather than a mechanism for selection of a zonal phase speed.
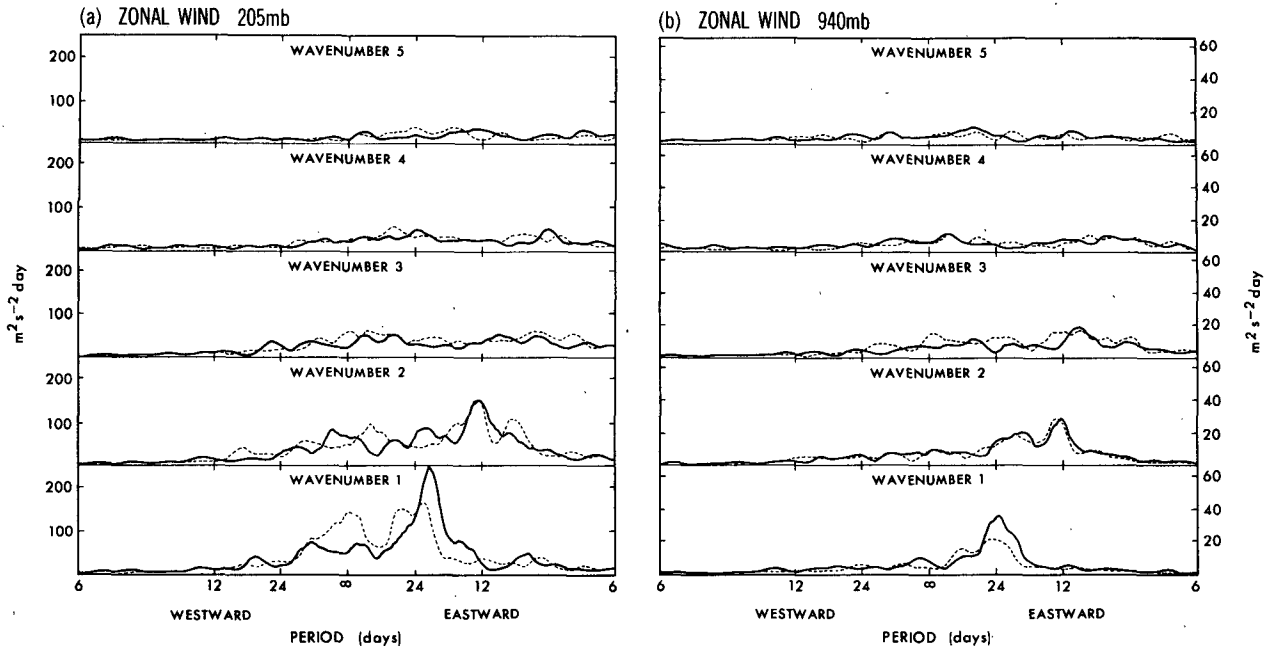
FIG. 1. Variance spectra of the equatorial zonal wind at (a) 205 and (b) 940 mb for zonal wavenumbers 1–5. The model data have been averaged over the two grid points at 2.25°N and 2.25°S. The solid and dashed lines represent the spectra for the first and second 700 days of the integration, respectively. Eastward- and westward-propagating variances are plotted on the right and left halves of the x-axis, respectively.

The variance of the zonally averaged zonal wind at the equator is found to be more than an order of magnitude smaller than the variance in zonal wavenumber one in this model. There *is* a significant zonally symmetric component to this oscillation in the GCM with realistic geometry analyzed by Hayashi and Golder
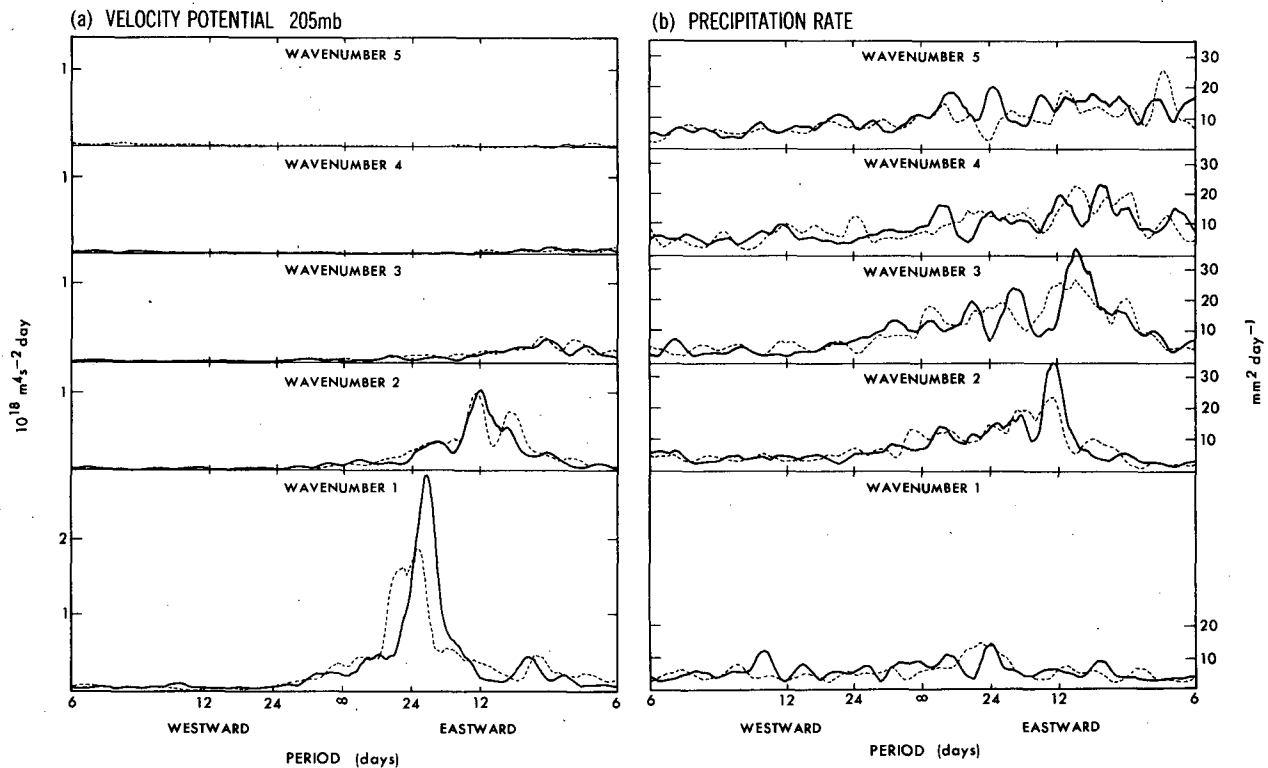

FIG. 2. As in Fig. 1, but for (a) velocity potential at 205 mb and (b) precipitation rate.

(1986, Fig. 4a). In the atmosphere this zonally symmetric component is reflected in changes in the rotation rate of the planet (Madden 1987). The implication is that a wavelike oscillation exists in the absence of zonal asymmetries in the boundary conditions but that these asymmetries modify the oscillation so as to produce a zonally symmetric component. In particular, one expects the *zonally averaged* latent heating to increase when the wave's region of rising motion passes over areas where the environment is particularly favorable for convection, such as the Indonesian sector.

A number of observational and GCM studies focus on the velocity potential associated with the Madden–Julian oscillation (Lorenc 1984; Knutson and Weickmann 1987; Lau and Lau 1986). The spectra of the model's velocity potential in Fig. 2a show that a larger fraction of the total variance resides in wavenumber 1 than is the case for the zonal wind perturbations. These spectra are in sharp contrast to those of the precipitation in Fig. 2b, in which one sees hardly any enhancement of power in wavenumber 1 but substantial power in eastward-moving disturbances in waves 2–5. These dif-
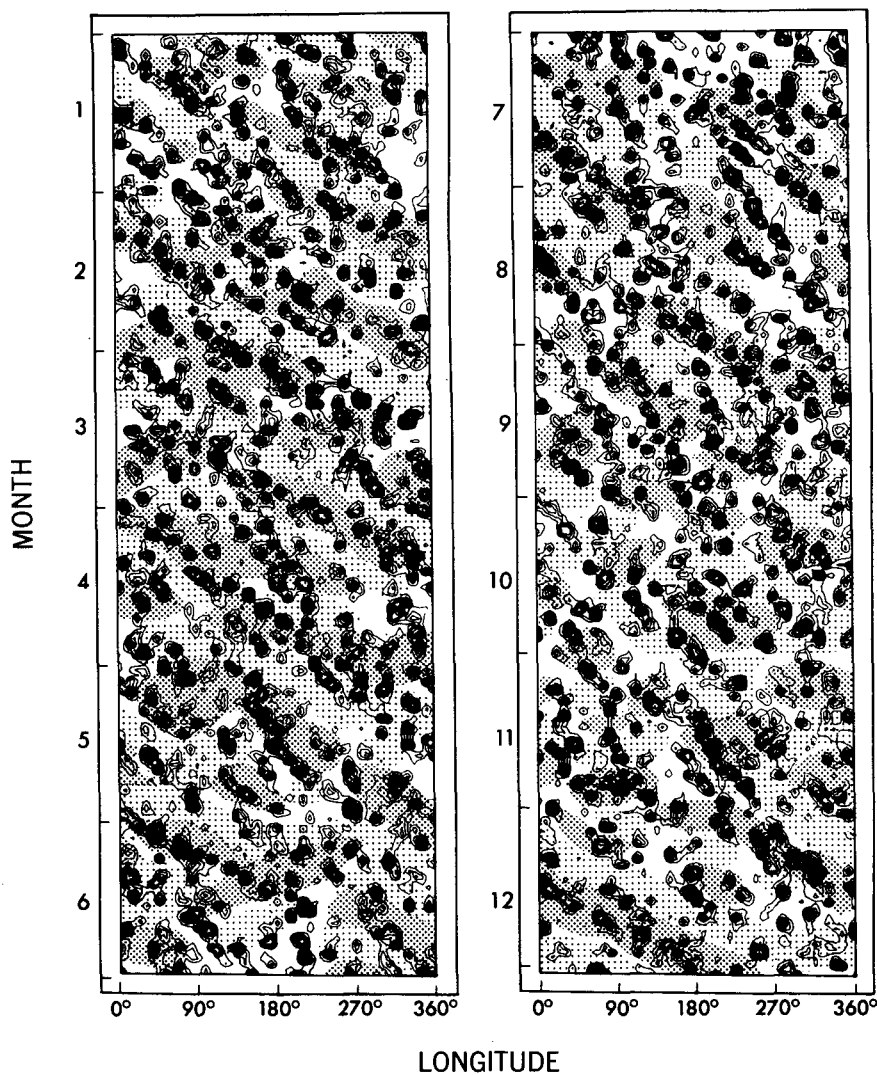

FIG. 3. Time–longitude distribution of precipitation rate (contour interval 4 mm d^{-1}) for a 12-month period of the model integration. Dense stippling indicates large-scale, upper-level divergence, with 205 mb velocity potential values less than -2×10^6 m^2 s^{-1}. Light stippling denotes large-scale, upper-level convergence, with 205 mb velocity potential exceeding 2×10^6 m^2 s^{-1}. The precipitation data are sampled at daily intervals and have been averaged over the four grid points between 6.75°N and 6.75°S. The velocity potential data have been subjected to the 10–40 day band pass time filter described in Fig. 5, and smoothed in the longitudinal direction by retaining only the first three zonal wavenumbers. The sampling interval for the velocity potential is three days, and the values shown are based on averages over the eight grid points between 15.75°S and 15.75°N. The time–space evolution of the filtered velocity potential field is essentially identical to that portrayed by the contour plot in the left panel of Fig. 4.

ferences in spectra are to be expected for a Kelvin wave–like oscillation, for which $D \propto \partial_x u \propto \partial_{xx} X$, where D is the divergence and X the velocity potential. Assuming that the shape of the precipitation spectrum is similar to that of D, it should be proportional to k^4 times the spectrum of X, where k is the zonal wavenumber. A Kelvin wave–like oscillation will stand out above a noisy background at low wavenumbers in velocity potential and higher wavenumbers in divergence and precipitation. Wavenumber 2 has a peak in its precipitation spectrum at a phase speed of 18–20 m s^{-1}, but the higher wavenumbers have broad spectra that tend to be dominated by somewhat lower speeds.

Another view of these eastward-moving disturbances can be seen in Fig. 3, a longitude–time plot of the model's precipitation averaged between 6.75°N and 6.75°S. The rainfall accumulated over each day is plotted for one year, with no additional spatial or temporal smoothing. Also shown by the stippling is the 205 mb velocity potential at the equator (smoothed as described in the following paragraph). Dense and light stippling indicate negative velocity potential (large-scale upper-level divergence) and positive velocity potential (convergence), respectively. Unlike the result of Hayashi and Sumi, who used a model with a Kuo-type convective parameterization instead of a convective adjustment scheme, the small-scale precipitation features do not propagate steadily at the same speed as the large-scale disturbance; rather, they seem to redevelop in regions favored by the large-scale convergence field (note the collocation of precipitation contours with dense stippling in Fig. 3). The characteristic speed associated with this downstream redevelopment is approximately 18 m s^{-1}. Individual features often propagate at slower speeds (e.g., month 5 near 180° longitude), reflecting the tendency toward slower speeds at higher wavenumbers in the precipitation spectra.

Figure 4 is plot of the 205 mb velocity potential averaged from 15.75°N to 15.75°S for three years of our integration. Only the first three zonal wavenumbers have been retained. The velocity potential has also been subjected to a bandpass filter with half power points at periods of 10 and 40 days, which encompass the spectral peaks in wavenumbers 1 and 2. The coefficients of the filter are listed in Table 1, and its frequency response for data sampled at three-day intervals is illustrated in Fig. 5. The first year of the velocity potential evolution is essentially identical to that shown by the stippling in Fig. 3. In many instances (e.g., months 12–13, 16, 20–21, 25–26, 31–32, 35–36) the large-scale disturbance remains coherent after traveling more than once around the equator.

3. Composite scheme

The composite procedure used here allows one to define the structure of the oscillation efficiently, and, given the episodic character of the phenomenon evident in Fig. 4, it also has the advantage of allowing one to focus on those time periods during which the oscillation is strong. The band-pass filtered 205 mb velocity potential field is used to define the spatial phase of the oscillation. Other fields of interest are then composited with respect to this phase. The details of the procedure are as follows:

Step 1: For each time instant t we average the band-pass filtered values of the 205 mb velocity potential over the latitude span from 15.75°N to 15.75°S, retaining only the first three zonal harmonics. These values are identical to those plotted in Fig. 4. The amplitudes of the Fourier sine and cosine components are denoted as s_i and c_i, where $i = 1, 2, 3$.

Step 2: The longitudinal phase of the oscillation at time t is established by finding the longitudes $\lambda^+(t)$ and $\lambda^-(t)$, which respectively correspond to the maximum and minimum in the filtered velocity potential data obtained in step 1.

Step 3: We denote a bandpass filtered model field (i.e., wind, geopotential, etc.) by $X(\lambda, \theta, t)$, where λ is longitude and θ latitude. We now translate this field in the zonal direction by $\Delta\lambda^+(t) = \lambda^+(t) - \lambda_0$, where λ_0 is a fixed reference longitude. Referring to the translated field as X_T^+, we have $X_T^+(\lambda, \theta, t) = X(\lambda + \Delta\lambda^+, \theta, t)$. If we choose X to be the velocity potential X, this translation aligns the maximum in X with the reference longitude λ_0. We repeat this process to align the minimum in the velocity potential with λ_0, i.e.,

$$X_T^-(\lambda, \theta, t) = X(\lambda + \Delta\lambda^-, \theta, t),$$

$$\text{where} \quad \Delta\lambda^- = \lambda^-(t) - \lambda_0.$$

Step 4: Step 3 is repeated for each time t (at three-day intervals) and the composite field $X^*(\lambda, \theta, 0)$ is defined as the following weighted average of the difference between X_T^+ and X_T^-:

$$X^*(\lambda, \theta, 0)$$
$$= W^{-1} \sum_t [X_T^-(\lambda, \theta, t) - X_T^+(\lambda, \theta, t)] w(t)$$

where

$$w(t) = \left[\sum_i (c_i^2 + s_i^2) \right]^{1/2} \quad \text{and} \quad W = \sum_t w(t).$$

The coefficients c_i and s_i have been defined in step 1. This weighting factor emphasizes periods with strong velocity potential fluctuations. Since the difference between X_T^- and X_T^+ has been taken in computing X^*, the latter should be interpreted as the peak-to-peak amplitude of the fluctuation.

Step 5: We refer to the result of step 4 as the *zero-lag composite*. In order to depict the transient evolution of the circulation patterns, steps 3–4 have been repeated using temporal lags or leads, so that the data fields being composited and the longitude shifts $\Delta\lambda^+$, $\Delta\lambda^-$
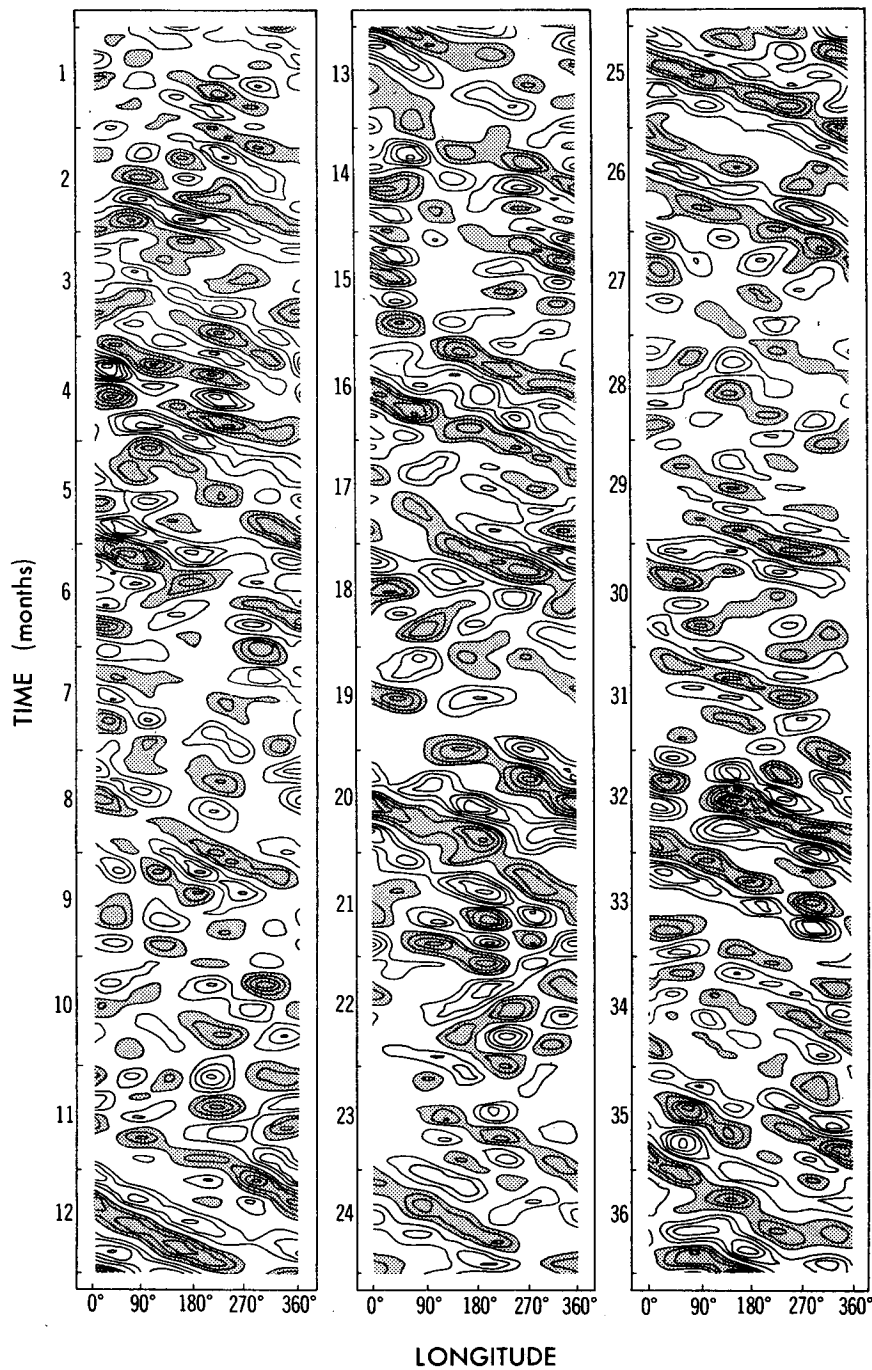
205mb VELOCITY POTENTIAL

TIME (months)

LONGITUDE

FIG. 4. Time–longitude distribution of 205 mb velocity potential for a 36-month period of the model integration. Contour interval: 2×10^6 m^2 s^{-1}. The zero contour is omitted for the sake of clarity. Stippling indicates values less than -2×10^6 m^2 s^{-1}. The model data have been averaged between 15.75°N and 15.75°S and filtered in time and space by retaining the 10–40 day periods and the first three zonal wavenumbers. The first 12 months in this plot correspond to the same period described in Fig. 3.
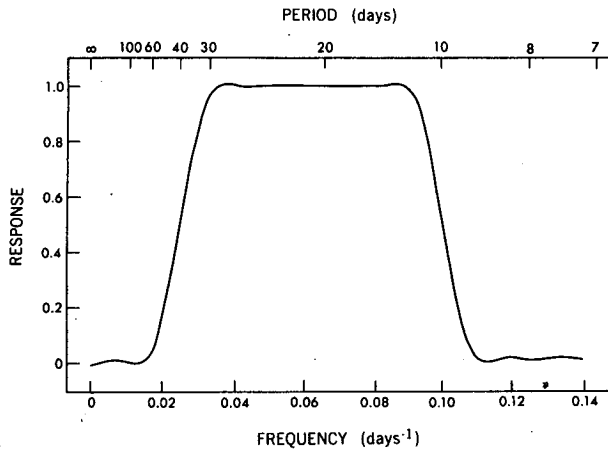
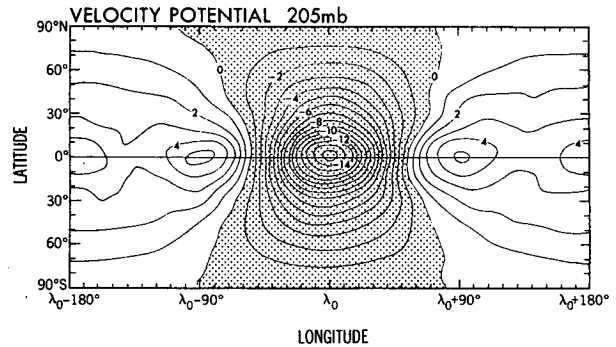FIG. 5. Response of the 10–40 day band-pass filter used in this study.

FIG. 6. Longitude–latitude distribution of the GCM composite at zero lag of the velocity potential field at 205 mb. Contour interval: 1×10^6 m^2 s^{-1}. Stippling indicates negative values. The reference longitude λ_0 is placed in the middle of the x-axis.

correspond to different times. For a given time lag or lead τ, the nonzero-lag composites are computed as

$$X^*(\lambda, \theta, \tau) = W^{-1} \sum_t [X_T^-(\lambda, \theta, t + \tau)$$

$$- X_T^+(\lambda, \theta, t + \tau)] w(t),$$

where $X_T^\pm(\lambda, \theta, t + \tau) = X(\lambda + \Delta\lambda^\pm(t), \theta, t + \tau)$. For positive (negative) values of τ, the composite $X^*(\lambda, \theta, \tau)$ can be interpreted as the typical structure of the oscillation at a time interval τ after (before) the arrival of the 205 mb velocity potential signal at the reference longitude λ_0.

4. Three-dimensional structure

a. Horizontal structure

To establish a framework for interpreting various fields constructed using this composite procedure, Fig.

TABLE 1. Coefficients for the 10–40 day band-pass filter used in this study. For a time series $X(t)$, the filtered value at time t_0 is given by

$$X(t_0) = c_0 X(t_0) + \sum_{i=1}^{19} c_i [X(t_0 + i\Delta t) + X(t_0 - i\Delta t)],$$

where $\Delta t = 3$ days is the data-sampling interval.

	Coefficients		Coefficients
c_0	0.450000	c_{10}	0.021908
c_1	0.157661	c_{11}	0.033733
c_2	−0.219171	c_{12}	0.000000
c_3	−0.161890	c_{13}	0.005469
c_4	0.000000	c_{14}	0.006710
c_5	0.041152	c_{15}	−0.006036
c_6	−0.058703	c_{16}	−0.013101
c_7	0.028321	c_{17}	−0.002188
c_8	0.037000	c_{18}	−0.000942
c_9	−0.001574	c_{19}	−0.004533

6 shows the zero-lag composite of the velocity potential itself. The reference longitude λ_0 is located in the middle of the longitude axis. There is naturally a minimum along the equator at λ_0. The maxima are displaced 90° and 180° from this minimum, reflecting the dominance of wavenumbers 1 and 2 in the velocity potential fluctuations. An analogous composite based on 830 mb data (not shown) bears a strong resemblance to this pattern, except for a sign reversal. In examining the composite charts to follow, it is helpful to keep in mind that ($\lambda = \lambda_0, \theta = 0$) is the center of the divergence in the upper troposphere and the center of convergence just above the boundary layer.

The zero-lag composites for the horizontal wind and pressure perturbations are shown in Fig. 7. Plotted are the horizontal wind vector (arrows) and geopotential height (contours) at (a) 205, (b) 830, and (c) 990 mb. The equatorial oscillation is clearly symmetric about the equator. Since the Northern and Southern Hemispheres in the GCM are physically identical, the degree of symmetry of these patterns is a measure of the statistical significance of the composite fields. Within the deep tropics, the geopotential perturbation in the lower troposphere (Figs. 7b and 7c) is negative east of the reference longitude λ_0 and positive to the west. These low- and high-pressure centers along the equator are labeled L_0 and H_0 in the figures. The subtropical regions to the north and south of the equatorial low L_0 at low levels are generally characterized by positive pressure fluctuations. Also evident in the patterns at 830 and 990 mb are two secondary low-pressure centers (labeled L_N and L_S) located northwest and southwest of L_0. We have found in examining this and other models with various filters that these subtropical cyclones become more prominent if the filter is shifted to lower frequencies.

The equatorial pressure pattern at 205 mb (Fig. 7a) is negatively correlated with that in the lower troposphere, with positive (negative) pressure to the east (west) of λ_0. Situated north and south of H_0 are two
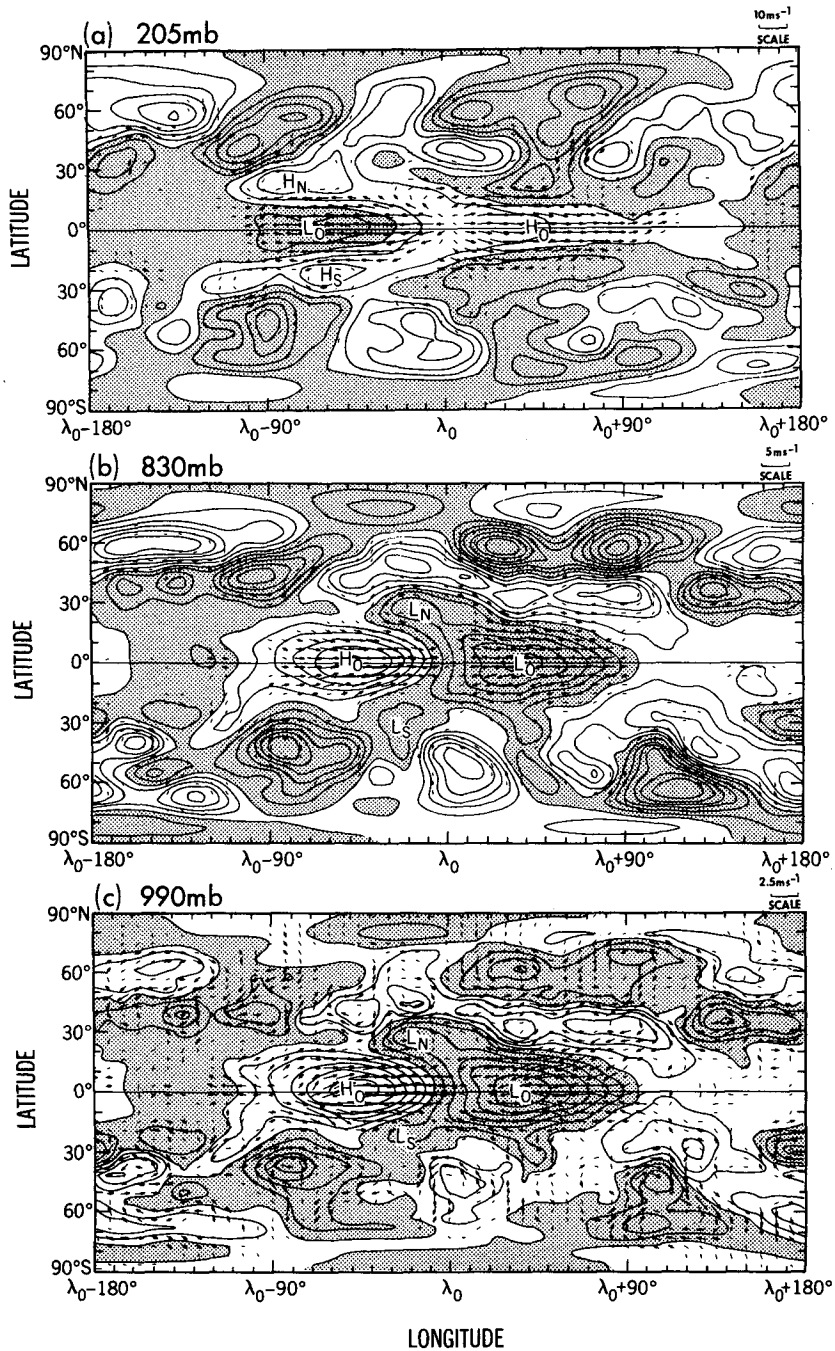
FIG. 7. As in Fig. 6, but for the GCM composites of the geopotential height (contours) and horizontal wind vector (arrows) fields at (a) 205, (b) 830, and (c) 990 mb. Contour interval is 5 m for 205 mb data and 2 m for 830 and 990 mb data. Stippling indicates negative height perturbations. The scales for the wind vectors are indicated at the top right corner of each panel. Arrows too short to show up clearly have been omitted. The labels H_0, H_N, H_S, L_0, L_N and L_S refer to high and low pressure centers discussed in the text.

elongated low-pressure zones, whereas a pair of high-pressure centers (H_N and H_S) are discernible to the north and south of L_0.

The extratropical patterns in Fig. 7 are less symmetric about the equator than the tropical features,

indicating less statistical significance. The signals in the extratropics are generally equivalent barotropic. Perhaps the best defined feature is the low at 205 and 830 mb located at $\lambda_0 - 90°$ and 40°N or S. The amplitude of this extratropical response is small ($\approx$20–30 m). In

observations (Lau and Phillips 1986) and in GCMs with realistic boundary conditions (Lau and Lau 1986), the extratropical response to this tropical oscillation tends to be larger, geographically fixed, and confined to the winter season. In view of the idealized geometry and annual mean forcing used in the present study, we cannot expect this experiment to yield a realistic extratropical response.

At both 205 and 830 mb, the flow pattern between 15°N and 15°S is dominated by the zonal wind component, with strong divergence in the upper troposphere and convergence in the lower troposphere centered at λ_0. There is a much stronger meridional component at 990 mb. This meridional flow is directed

across the isobars from high toward low pressure. The resulting convergence into L_0 and divergence out of H_0 is presumably produced by the model's frictional stresses near the surface. The result is an eastward shift in the surface divergence as compared with the divergence above the boundary layer.

Some of the characteristics of the moist processes accompanying the tropical oscillation are illustrated by the zero time-lag composites in Fig. 8. Shown are (a) precipitation rate, (b) pressure velocity at 515 mb, (c) evaporation rate, and (d) water vapor mixing ratio at 940 mb. In view of the weak extratropical signal in these fields, the plotting domain is confined to the region between 45°N and 45°S. It is seen from Fig. 8a
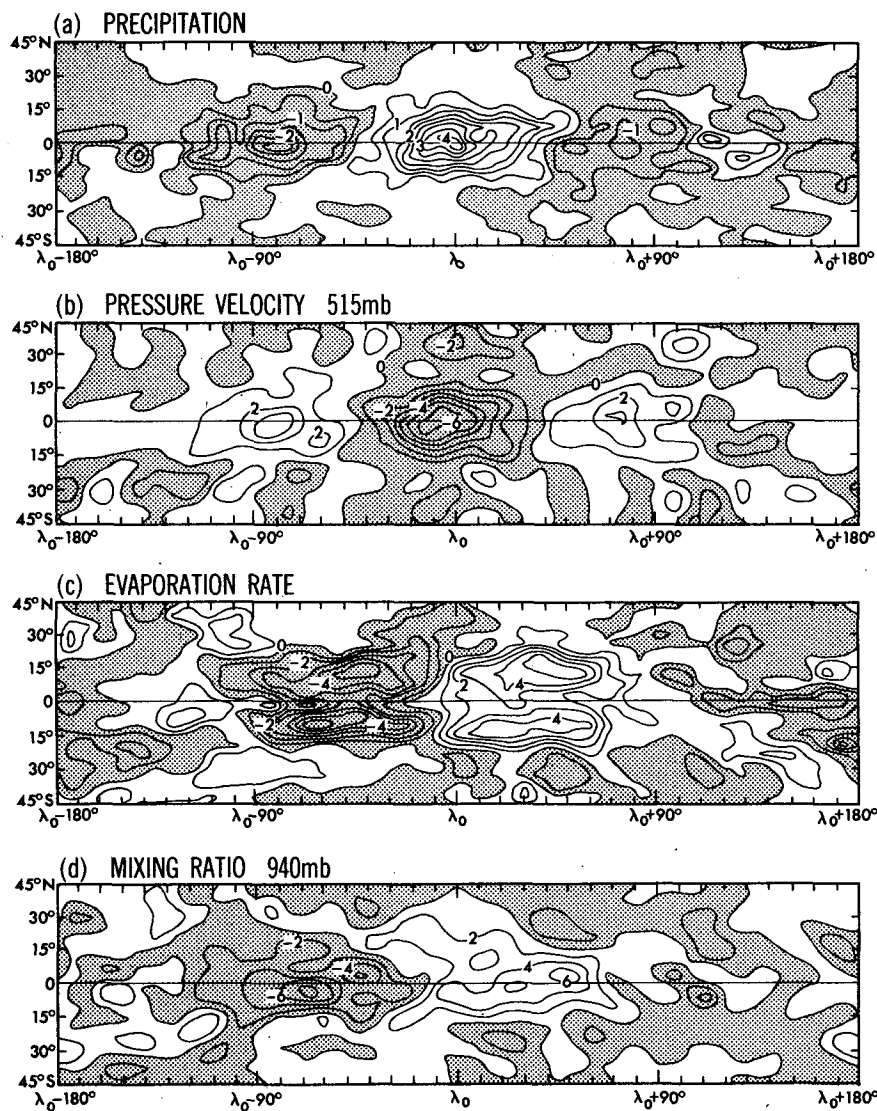

FIG. 8. As in Fig. 6, but for the GCM composites of (a) precipitation rate (contour interval: 0.5 mm d^{-1}), (b) pressure velocity at 515 mb (contour interval: 10^{-2} Pa s^{-1}), (c) evaporation rate (contour interval: 0.1 mm d^{-1}) and (d) water-vapor mixing ratio at 940 mb (contour interval: 2 × 10^{-4}). Stippling indicates negative values. Only values between 45°S and 45°N are plotted.

that an elongated precipitation maximum is centered near λ_0. This feature extends from approximately 10°N to 10°S and has a longitudinal span of about 60°. East and west of the precipitation zone are regions of suppressed rainfall. As seen in Figs. 2b and 3, the precipitation making up this pattern actually encompasses a wide range of space and time scales and takes the form of small cores that tend to develop in regions favored by the large-scale divergence field. The structure of this precipitation composite may be sensitive to the details of the composite procedure, particularly to the time-filtering of the precipitation and the velocity potential used to define the reference longitude.

There is a very close correspondence between the precipitation pattern and the pattern of midtropospheric vertical motion (Fig. 8b), with little or no longitudinal phase shift between the two. In contrast, the evaporation and mixing ratio composites *are* noticeably shifted with respect to the precipitation and vertical motion. The fluctuations in mixing ratio reach their maximum positive values east of λ_0 along the equator. Comparison with the 990 mb height composite in Fig. 7c reveals that high water-vapor mixing ratios are associated with low-pressure centers (L_0, L_N, and L_S in Fig. 7c) and horizontal convergence near the lower boundary, and low mixing ratios with the surface high H_0 and divergence.

The evaporation also reaches its highest values to the east of λ_0, but off the equator at $\approx 10°$ latitude in both hemispheres. Evaporation in the GCM is computed from the mixing ratio and wind speed at the surface using the bulk formula. Since the positive mixing ratio anomaly (see Fig. 8d) to the east of λ_0 acts to depress local evaporation, the increase in evaporation between λ_0 and $\lambda_0 + 60°$ must be due to the increased wind speed resulting from the superposition of the anomalous easterlies (Fig. 7c) on the mean easterlies in the tropics. The peak off the equator is related to the presence of "noise" in the atmospheric winds and the dependence of the evaporation on the wind *speed* (i.e., the nonlinear dependence on the wind itself). The mean surface easterlies increase in strength from 1–2 m s^{-1} near the equator to 5–6 m s^{-1} at 15° latitude, so the atmospheric noise changes the sign of the zonal wind less often off the equator. As a result, the superposition of the oscillation onto the mean flow plus noise will more consistently produce an evaporation anomaly of a given sign off the equator.

The evaporation anomalies are only one-fifth to one-tenth as large as the precipitation anomalies, but in the delicately balanced tropical atmosphere modest gradients in the evaporation can have significant effects on the evolution of the convective activity, as argued by NHC and Emanuel (1987). Indeed, NHC show that the removal of the wind speed dependence in this GCM's formula for evaporation (the instantaneous wind speed being replaced by its climatological value) substantially reduces the amplitude of the eastward–

propagating power in the zonal flow at periods from 8 to 40 days.

When this evaporation-wind feedback is removed, the reduction in power in the higher wavenumbers that dominate the precipitation spectrum is less dramatic than that shown in NHC for the wavenumber 1 and 2 components of the zonal wind. Figure 9 shows the space–time spectrum of equatorial precipitation in the GCM in which the wind speed dependence of evaporation has been removed (the "fixed-V, fixed SST" model in the terminology of NHC). This figure can be compared to the corresponding spectrum in the standard experiment (Fig. 2b). A preponderance of eastward-propagating, low-frequency power is evident in both models, with the power being reduced by about 30% in the "fixed V" experiment. Also, the wavenumber 2 spectral peak at a period of 12 days in the standard model is less distinct in the "fixed V" case. It is unclear why the evaporation-wind feedback has a stronger effect on the zonal wind spectra.

It is possible that the low-level mixing ratio anomalies are also dynamically significant, despite their small size (at most 0.7×10^{-3}). On the one hand, the positive anomaly east of the heating could help damp eastward-propagating waves by reducing the evaporation anomaly; on the other hand, the slight increase in the conditional instability east of λ_0 could enhance the amplitude of eastward-propagating disturbances.

b. Vertical structure

The circulation in the equatorial zonal plane accompanying these oscillations is portrayed in Fig. 10,
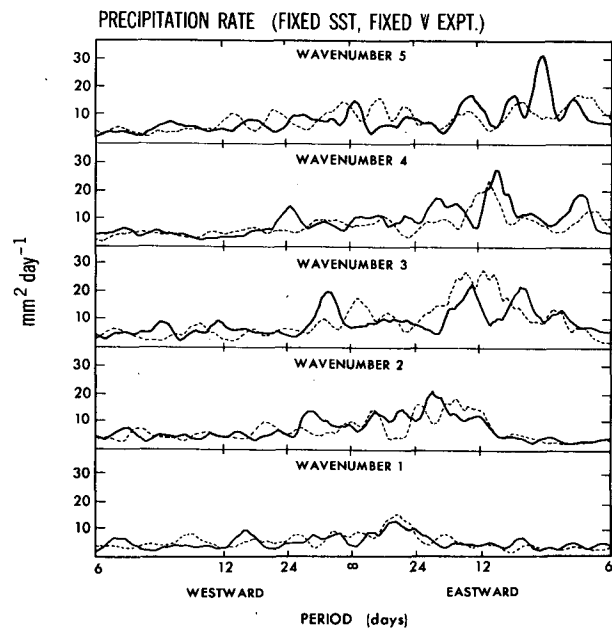

FIG. 9. As in Fig. 2b, but for the precipitation data from a GCM integration in which the wind speed dependence of evaporation has been removed.

which shows the longitude–pressure distribution of the zero-lag composite data, averaged over the ±2.25° latitude grid points, for (a) zonal wind, (b) pressure velocity, and (c) net heating due to latent heat release and moist convective mixing. Figure 10a shows that the maximum inflow toward λ_0 occurs at the 830 mb level and maximum outflow at 205 mb, with the transition from westerlies to easterlies at a given longitude occurring near 500 mb. The zonal wind amplitudes near the tropopause are larger than those in the lower
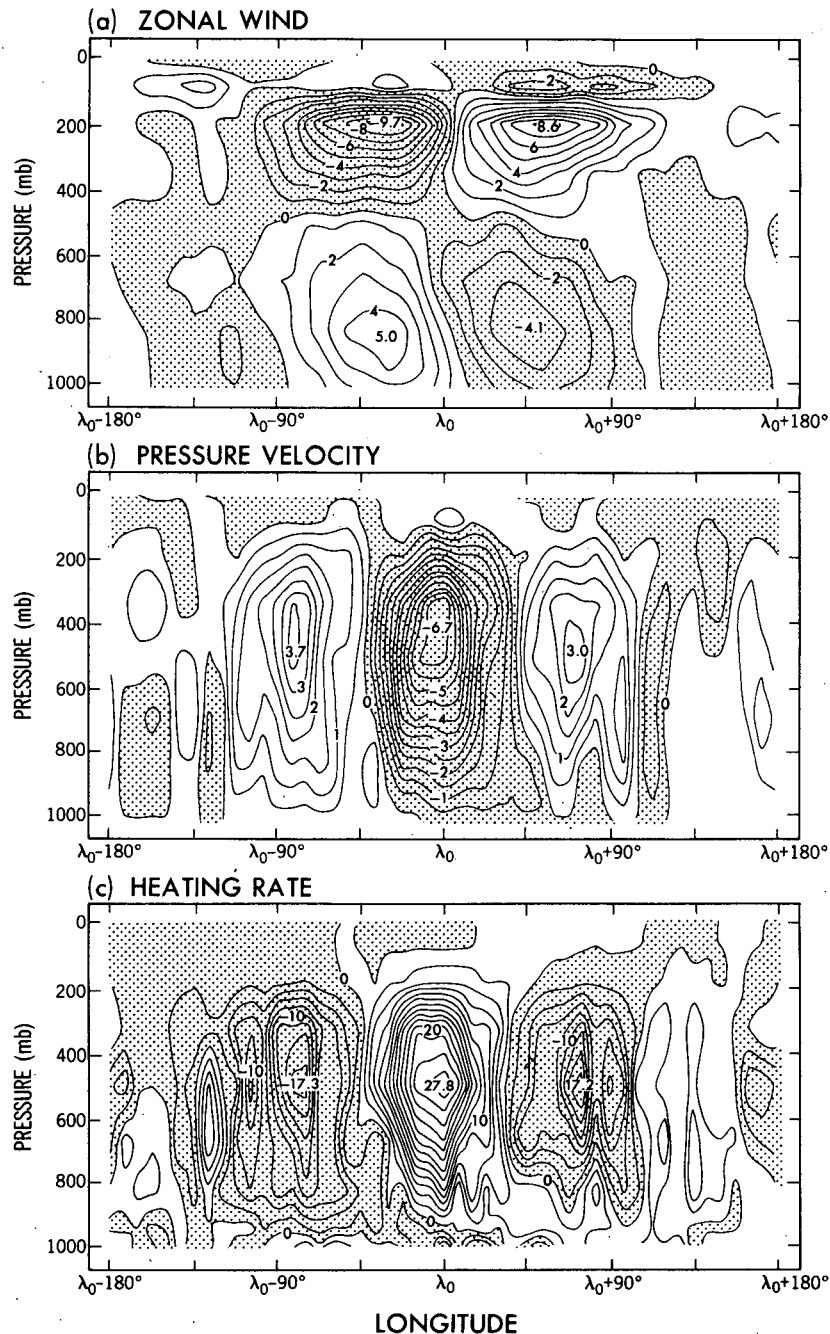

FIG. 10. Longitude–pressure distribution of the GCM composites at zero lag of (a) zonal wind (contour interval: 1 m s^{-1}), (b) pressure velocity (contour interval: 5 × 10^{-3} Pa s^{-1}) and (c) heating rate due to latent heat release and moist convective mixing (contour interval: 2 × 10^{-6} °C s^{-1}). The model data have been averaged over the two grid points at 2.25°S and 2.25°N. Stippling indicates negative values. The reference longitude is placed in the middle of the x-axis.

troposphere. The vertical velocity (Fig. 10b) that closes this circulation bears a close similarity to the heating field (Fig. 10c), indicating the dominant balance in the thermodynamic equation between latent heating and adiabatic cooling. All three panels in Fig. 10 exhibit westward tilts with increasing altitude near the surface.

There is a hint of this behavior in Murakami and Nakazawa's (1985) estimate of the observed vertical structure of the oscillations based on FGGE analyses.

The vertical structure of the equatorial fluctuations in other variables of interest is shown in Fig. 11. Included are (a) geopotential height, (b) temperature,
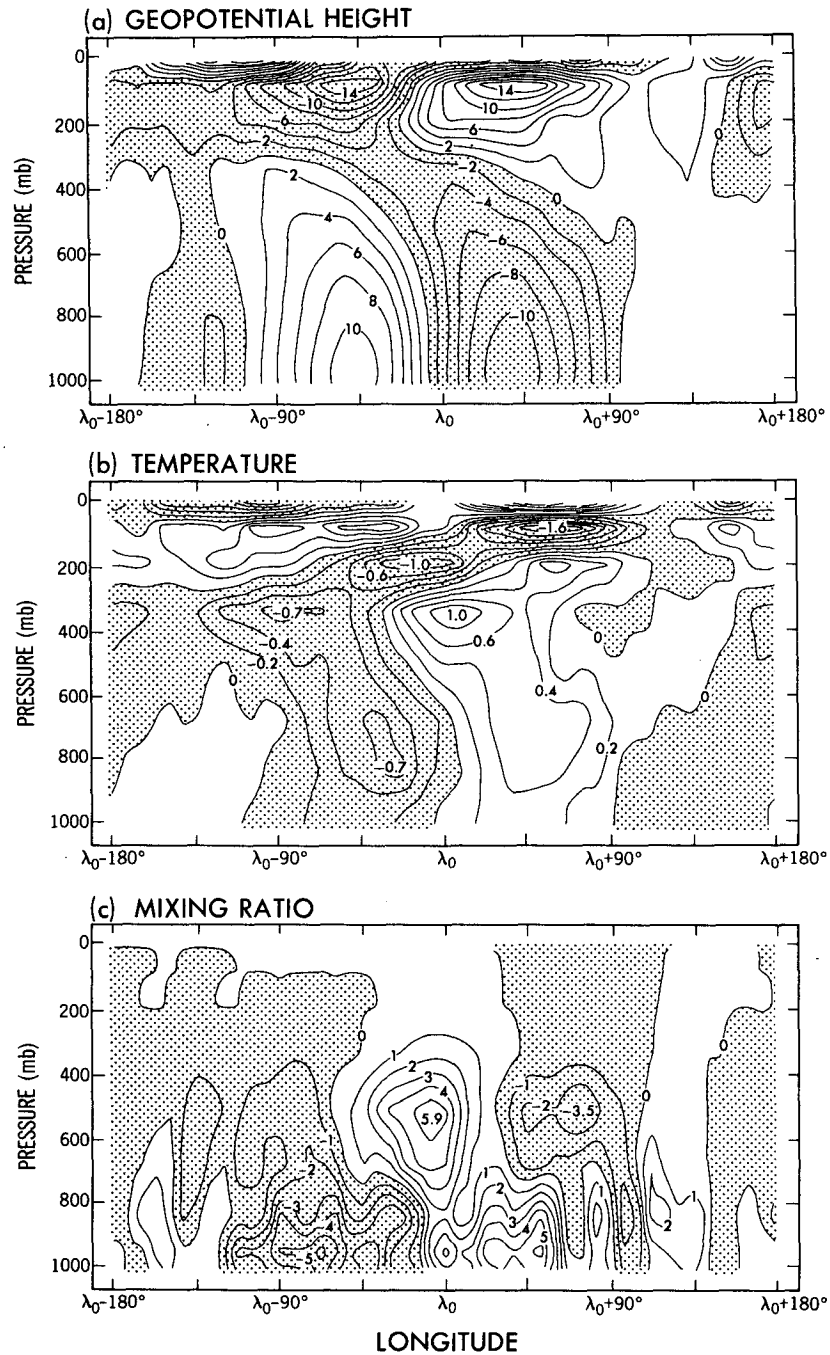

FIG. 11. As in Fig. 10, but for the GCM composites of (a) geopotential height (contour interval: 2 m), (b) temperature (contour interval: 0.2°C) and (c) water-vapor mixing ratio (contour interval: 1×10^{-4}).

and (c) water-vapor mixing ratio. If one linearizes the zonal equation of motion about a state of rest, neglecting damping,

$$\partial u/\partial t = fv - \partial \Phi/\partial x, \tag{1}$$

then the balance at the equator ($f = 0$) is simply between the zonal wind tendency and the geopotential gradient. If the disturbance is neutral and has a well-defined phase speed, then one expects the u and Φ patterns to be identical. The differences between Figs. 10a and 11a are therefore of interest. The decrease in the magnitude of u but not Φ as the surface is approached is presumably due to boundary-layer mixing. The differences at upper levels are more surprising; the maximum in the geopotential perturbations occurs near 100 mb, as opposed to 200 mb for the upper-level zonal wind. Nonlinearity of some kind, perhaps related to wave breaking, must be invoked to explain this difference. The slight longitudinal phase shift of Φ behind u at upper levels is suggestive of a growing wave (e.g., Wang 1988, Fig. 4).

The temperature fluctuations are weak (less than 1°C). There is a westward tilt with height between 830 and 350 mb, with the result that in the lower troposphere the temperature perturbation is in quadrature with the heating field, while in the upper troposphere it is almost in phase. There is some evidence for an increase in static stability west of λ_0 of the sort that plays an important role in Hendon's (1988) two-layer model. The eastward phase tilt with height in the stratosphere is suggestive of a Kelvin wave with upward group velocity, but the model clearly cannot resolve the small vertical wavelengths ($\approx$4–6 km) consistent with a phase speed of 15–20 m s^{-1}. Despite their different appearances in the stratosphere, the geopotential and temperature composites are consistent with hydrostatic balance.

The largest increase in the mixing ratio at low levels (Fig. 11c) occurs 30°–50° longitude east of λ_0, with drying of the atmosphere extending west of λ_0 for 120°. These changes in the moisture content at low levels are in phase with the temperature perturbations (see Fig. 11b). If the relative humidity were fixed, the mixing ratio at low levels would increase $\approx 1 \times 10^{-3}$ for each one degree increase in temperature. Therefore, roughly half of the low-level moisture changes can be explained by assuming fixed relative humidity. In contrast to the low-level pattern, there is moistening in the midtroposphere centered near λ_0. The contributions to the moist static energy are one possible measure of the relative importance of temperature and moisture perturbations for convective activity. Comparing $c_p T$ to Lr, where c_p is the heat capacity at constant pressure, and L the latent heat of vaporization, one finds the perturbations in Figs. 11b and 11c to be of the same order of magnitude, but with the moisture perturbations larger, particularly at low levels.

In order to explore the interesting longitudinal shift

near the surface evident in Figs. 7 and 11, we show in Fig. 12 the equatorial longitude–pressure distribution of the composited anomaly of horizontal divergence, $\nabla \cdot \mathbf{v}$, and the horizontal divergence of moisture, $\nabla \cdot (r\mathbf{v})$. Below 900 mb, the maxima in the convergence itself and in the moisture convergence are shifted $\approx$30° longitude east of λ_0. The perturbations in r are small enough that $\nabla \cdot (r\mathbf{v}) \approx r_0 \nabla \cdot \mathbf{v}$, where r_0 is the average mixing ratio in the model tropics, with a typical value of 1.5×10^{-2} below 900 mb. The shift in the low-level convergence is primarily due to the meridional frictional convergence into the surface low L_0 to the east of λ_0 (Fig. 7c). This shift between the longitude of the low-level moisture convergence and the latent heat release would not be captured in standard CISK models, in which heating at all levels is proportional to and in phase with the low-level convergence.

c. Temporal evolution

One can look for changes in the structure of this oscillation through its life cycle by compositing with different time lags as described in section 3. Examining the various composites, we find that all fields propagate at a phase speed of $\approx$18 m s^{-1} and that no changes in structure are clearly evident as a function of time. In view of the considerable variability in the duration of individual events, this compositing procedure is not able to isolate the structure of the disturbance in its initial amplifying stage.

As an example, Fig. 13 shows the equatorial precipitation and mixing ratio at 940 mb as a function of longitude and time lag. Lags of 0, ±3, ±6, ±9 and ± 12 days have been used to generate the figures. The data have been averaged over ±2.25° latitude, and a 1:2:1 longitudinal smoothing has been applied for each individual time lag. The peak in low-level moisture lies east of the precipitation maximum at all time lags and precedes the arrival of the precipitation at λ_0 by $\approx$3 days.

5. Linear response to the GCM's heating

In developing theories of this tropical oscillation, it is important to understand the extent to which linear theory can explain its structure, given the latent heating field. We address this question using a linear, primitive equation model on the sphere. A similar approach has been taken by Hayashi and Miyahara (1987). In the present study, the model described in Nigam et al. (1986) has been modified to allow for a uniformly propagating rather than stationary heat source. The model has the same finite-differencing in the vertical as the GCM but is unlike the GCM in that variations in the meridional direction are represented by finite differences rather than a spectral expansion. The three-dimensional forcing in the model is taken to be the net heating due to moist convection obtained from the composite procedure of section 3. The heating is as-
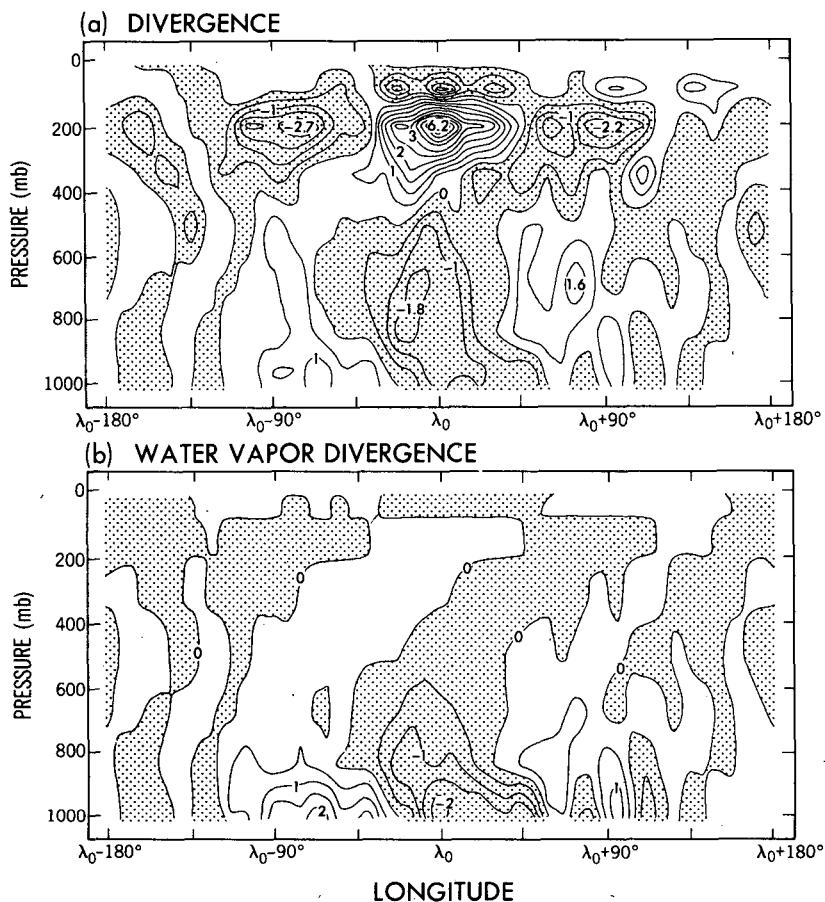
(a) DIVERGENCE

(b) WATER VAPOR DIVERGENCE

LONGITUDE

FIG. 12. As in Fig. 10, but for GCM composites of (a) horizontal divergence (contour interval: 5×10^{-7} s^{-1}) and (b) divergence of horizontal water-vapor transport (contour interval: 5×10^{-9} s^{-1}).

sumed to propagate eastward at 18 m s^{-1} and is symmetrized about the equator before being incorporated in the linear model. (This forcing is meant to represent that part of the heating that is coherent with the large-scale oscillations in the flow field. As described in section 2, the actual precipitation in the GCM is characterized by a broad range of space and time scales.) The model is linearized about the GCM's zonally symmetric climatology. In trying to simulate the GCM's oscillation, we obtain a better result if we include strong damping near the surface and the top of the linear model, and moderate damping in the interior. The coefficients of thermal damping and Rayleigh friction chosen are listed in Table 2. In addition, the mechanical damping is increased to large values at points where the phase speed of the wave matches the zonal flow, just as in Nigam et al. (1986).

The vertical structure in the equatorial plane produced by this linear model is shown in Fig. 14. The center of the heating, λ_0, is located at the center of the x-axis in each plot. The zonal velocity, geopotential, and temperature structures can be compared directly

with Figs. 10 and 11. Without the enhanced friction near the surface, the zonal wind perturbation has a similar structure to the geopotential, with a local maximum at the surface. Without the enhanced friction near the top of the model, the linear solution is large and noisy above the heating, as the model tries, with insufficient resolution, to resolve the small vertical scales of the free waves excited by such a moving source. Substantial noise remains in the temperature field, despite the strong damping. It is clear from the GCM composites that the disturbances above 200 mb are effectively being damped in the GCM also. Radiative damping can be efficient in attenuating such low-frequency fluctuations because of their small vertical group velocities (e.g., Garcia and Salby 1987), but the damping required by the linear model to mimic the GCM (Table 2) is much stronger than radiative damping could provide.

The linear model's damping at upper levels produces differences in the upper-tropospheric structures of the zonal wind and geopotential, with the upper-tropospheric geopotential maximum being located at a
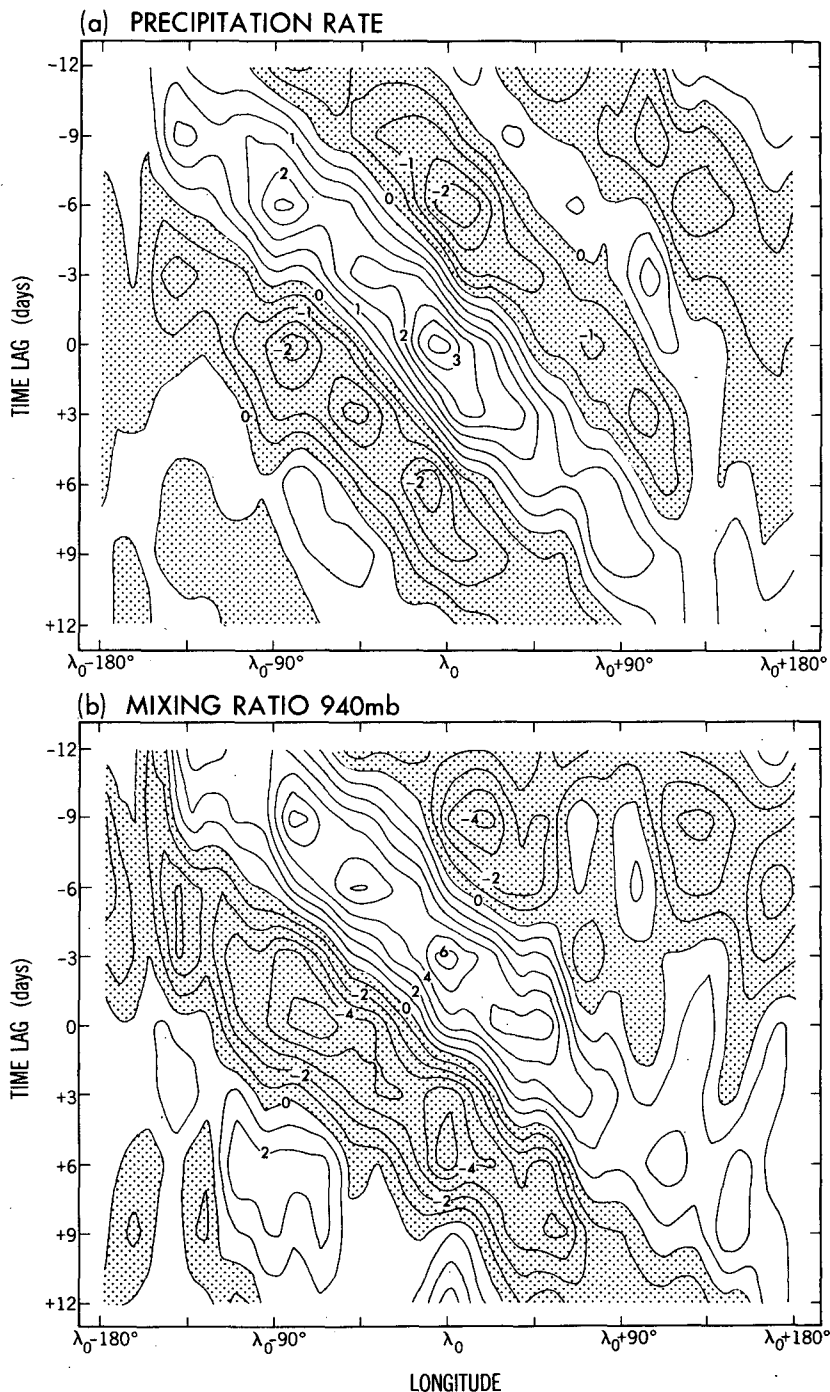
FIG. 13. Longitude–time distributions of the GCM composites of (a) precipitation rate (contour interval: 0.5 mm d^{-1}) and (b) water vapor mixing ratio at 940 mb (contour interval: 1×10^{-4}). Stippling indicates negative values. The model data have been averaged over the two grid points at 2.25°S and 2.25°N, and a 1:2:1 smoothing has been applied in the longitudinal direction. The reference longitude λ_0 is placed in the middle of the longitude axis.

greater height than the zonal wind maximum. However, the differences in structure are not as great as in the GCM (see Figs. 10a and 11a). The temperature field has the correct phase shift in the lower and middle troposphere, but its amplitude is larger than that in the GCM composite. Consistent with the larger tempera-

TABLE 2. The *e*-folding times (in units of days) for the Rayleigh friction, κ_M, and thermal damping, κ_T, used in the linear model of section 5.

σ-level	κ_M^{-1}	κ_T^{-1}
0.025	0.5	0.5
0.095	1.0	1.0
0.205	10.0	10.0
0.350	10.0	10.0
0.515	10.0	10.0
0.680	10.0	10.0
0.830	10.0	10.0
0.940	1.0	10.0
0.990	1.0	10.0

ture amplitudes, the geopotential changes sign at a lower level than in the GCM.

The horizontal structure of the linear model's response is shown in the left panels of Fig. 15. Comparison can be made with the GCM structures in Fig. 7 (noting that the contour interval for the geopotential is 2 m in Fig. 15 and 5 m in the upper panel of Fig. 7). Both the zonality of the upper-tropospheric equatorial winds and the meridional convergence at low levels are qualitatively captured. However, the extratropical geopotential response at 200 mb bears little resemblance to that in the GCM. A linear model with arbitrary damping near the critical surface is evidently unable to connect the wavy solution in the midlatitude region with the evanescent region in the tropics. At low levels, where critical lines should play a less important role, the extratropical response is more adequate. By examining the linear model solutions for various propagation speeds of the heat source, we have confirmed that the upper-tropospheric anticyclones to the west of the heat source (H_N and H_S in Fig. 7a) become more prominent in the linear response as the phase speed of the source is lowered.

The right panels in Fig. 15 show the eddy flow when the model is linearized about a state of rest rather than the GCM's climatology. The differences at low levels are small. At 200 mb, the extratropical response is now absent since the eastward-moving source can no longer excite Rossby waves, while the tropical geopotential response is now much wider, in disagreement with the GCM. When the model is linearized about a state of rest, the vertical structure in the equatorial plane (not shown) is altered hardly at all from that in Fig. 14.

Substantial damping is needed to obtain a satisfactory fit to the GCM, and even then the response is far from perfect. However, given the uncertainties in how to relate the convective heating to the large-scale flow, we feel that our results are sufficient to justify linearizing the momentum and temperature equations in idealized models of this phenomenon. One loses little by linearizing about a state of rest (although the mean flow could play a more significant role for the observed disturbance with its smaller phase speed).

6. CISK

Since linear dynamics yields considerable insight into the structure of the oscillation, given the heating, it remains to model the heating as a function of the large-scale flow and to determine how this coupling determines the characteristic phase speed. A wave-CISK formalism has been used in several recent papers in attempts to make this connection for the Madden–Julian oscillation (Lau and Peng 1987; Miyahara 1987; Takahashi 1987). In such a model, one fixes the vertical structure of the heating and sets its magnitude proportional to the low-level convergence. The problem of moisture availability is not addressed. The equations are linear if one further assumes "unconditional" heating, with negative heating anomalies being produced by low-level divergence. Unconditional heating is relevant when the disturbance creates small perturbations in a flow that is precipitating and does not reduce the precipitation to zero anywhere. Since the maximum in our composited rainfall is comparable to the mean rainfall along the equator (cf. Figs. 8 and appendix A), unconditional heating may not be appropriate for a model of this composite. That the modulation is not a small perturbation is also evident from Fig. 3. Lau and Peng (1987) and Hendon (1988) have emphasized the importance of conditional heating (positive heating only) for modeling translating clusters. Keeping these complications in mind, we consider only the linear problem with unconditional heating.

We linearize about a state of rest, as is partly justified by the results in section 5, and ignore spherical geometry as well as the nonseparability resulting from latitudinal dependence in the low-level moisture content. Finally, we consider only the Kelvin wave part of the dispersion relation, with zero meridional velocity, guided by the strong similarity of the composite oscillation to such a wave. The result is a simple gravity- or Kelvin-wave CISK model:

$$\left. \begin{aligned} \partial_t u &= -\partial_x \Phi \\ \partial_t T &= -\omega(\partial_p \bar{T} - \kappa \bar{T}/p) + Q/c_p \\ \partial_x u &= -\partial_p \omega \\ \partial_p \Phi &= -RT/p \end{aligned} \right\} . \tag{2}$$

Subscripts denote differentiation; the notation follows standard meteorological conventions. We set $Q = Q_0 f(p)$ with

$$Q_0 = L\nabla \cdot \left(\int_0^{p*} r(p)\mathbf{v}(p)dp/p_* \right)$$

$$= -L \int_0^{p*} r(p)\partial_p \omega dp/p_*, \tag{3}$$

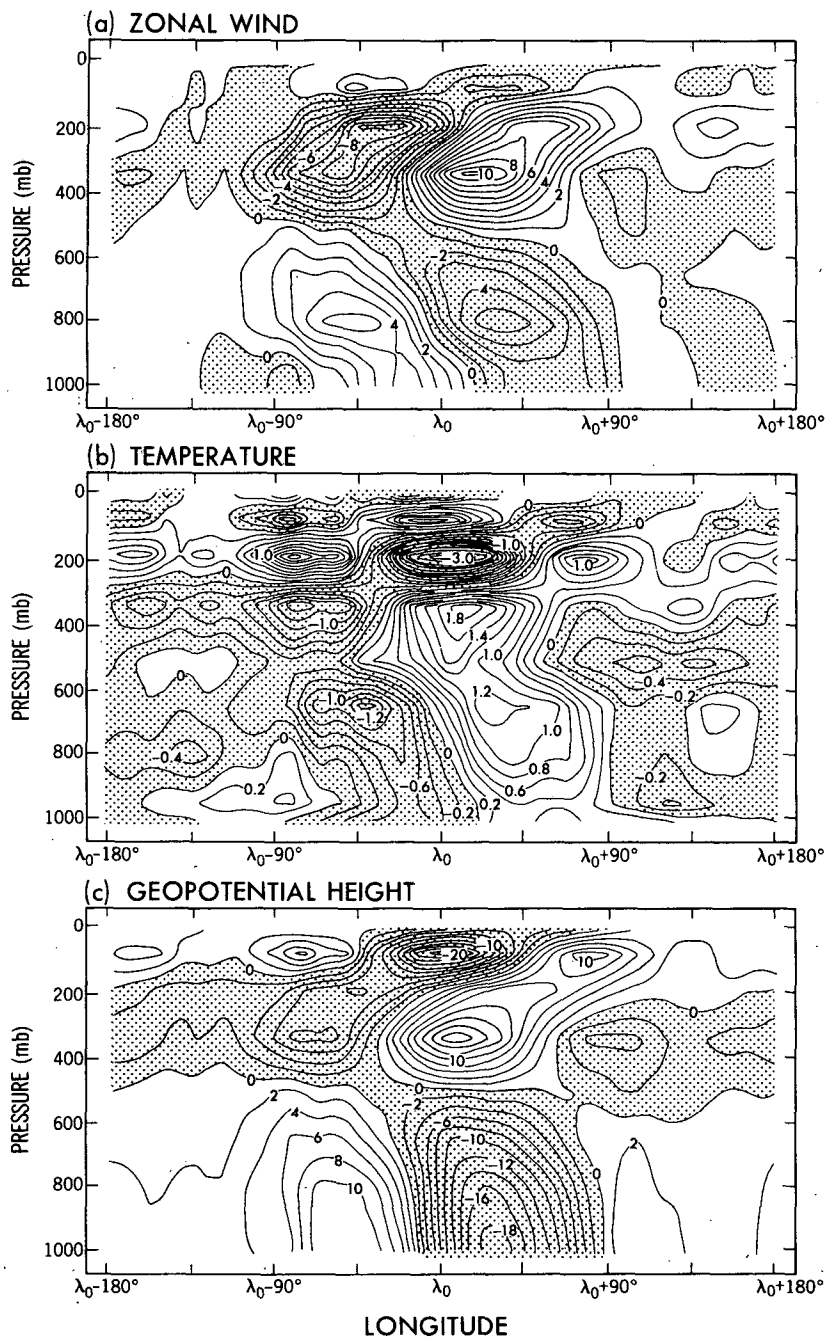$$\int_0^{p*} f(p)dp/p_* = 1, \tag{4}$$

FIG. 14. Longitude–pressure distribution at the equator of (a) zonal wind (contour interval: 1 m s^{-1}), (b) temperature (contour interval: 0.2°C) and (c) geopotential height (contour interval: 2 m), as obtained from the solution of the linearized model forced by a traveling heat source (described in section 5). Stippling indicates negative values. The center of the heating is located at the reference longitude λ_0 in the middle of the x-axis.

where $p_* = 1000$ mb. The moisture distribution is chosen by setting $r = r_0$ below 900 mb, $r = r_0/2$ between 760 and 900 mb, and $r = 0$ above 760 mb. A rough approximation to the moisture distribution in the GCM

results from the choice $r_0 \approx 15 \times 10^{-3}$. The vertical distribution of the diabatic heating $f(p)$, shown by the solid line in Fig. 16, is based on the structure of the heating in the GCM composite at the reference lon-
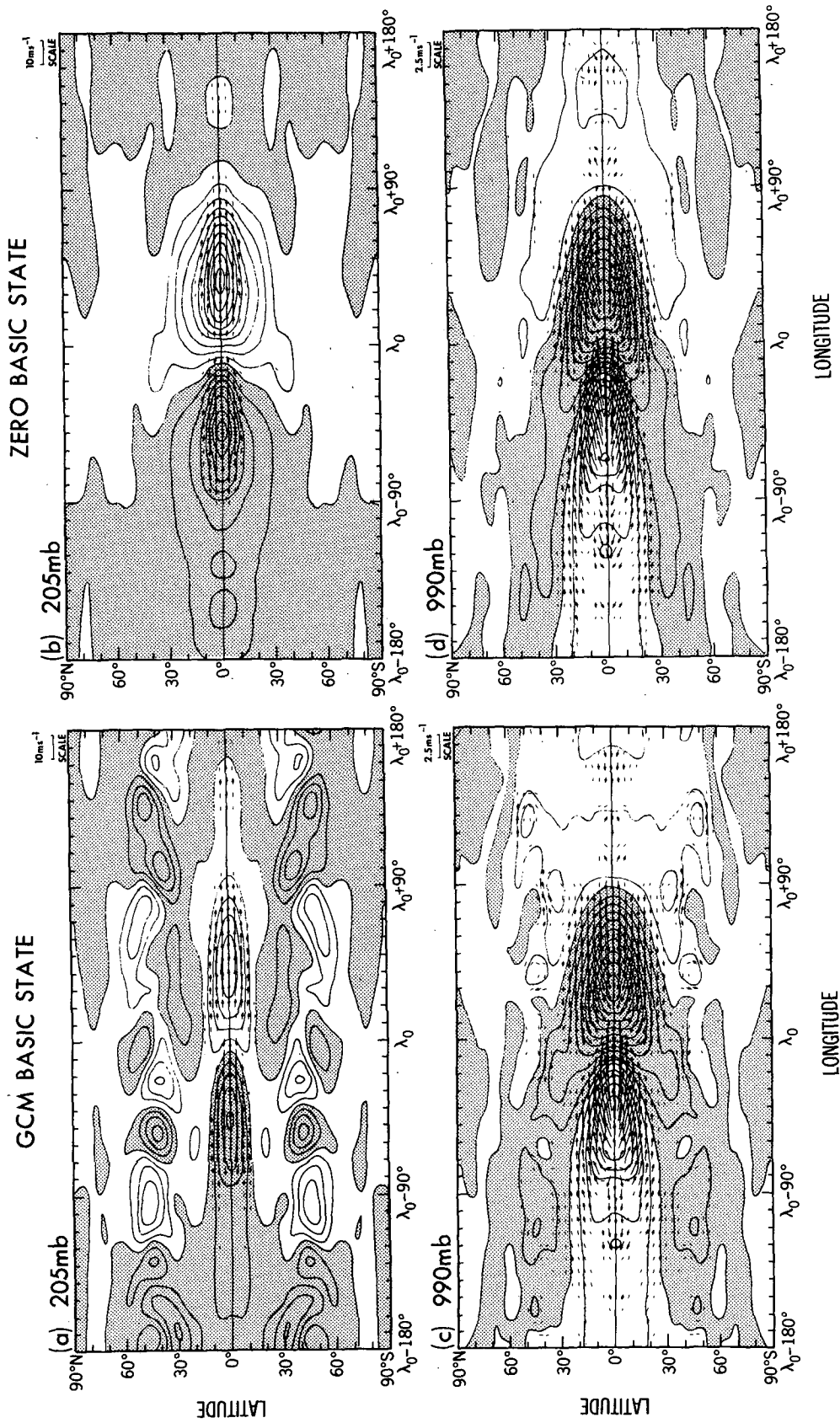
FIG. 15. Longitude–latitude distributions of the geopotential height (contours) and horizontal wind vector (arrows) fields at 205 mb (upper panels) and 990 mb (lower panels), as obtained from the linearized model forced by a traveling heat source (described in section 5). The model response when linearized about a basic state given by the climatology of the idealized GCM is displayed in the left panels; the response when linearized about a state everywhere at rest is shown in the right panels. Contour interval for all panels is 2 m. Stippling indicates negative height perturbations. The scales for the wind vectors are indicated at the top right corner of each panel. Arrows too short to show up clearly have been omitted.
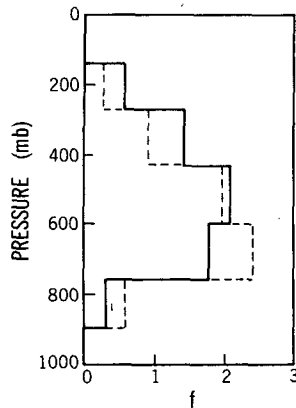
FIG. 16. The vertical distribution of the heating field used in the wave-CISK model to obtain the results described in section 6 (solid line), and a heating distribution that produces an unstable mode with phase speed closer to that of the observed oscillation (dotted line).

gitude λ_0. The vertical finite-differencing is exactly that of the GCM. Details of the differencing scheme can be found in appendix B.

We have not tried to include dissipation, either near the surface or near the model top, even though both were found to be useful in section 5 for the simulation of the perturbation flow, given the GCM's heating field. Since an amplifying wave will decay above the heated region, dissipation near the model top will be less important than for the steady waves generated in the linear model described in section 5. Furthermore, by setting $v = 0$ in this eigenvalue calculation, we have eliminated an important way in which the large damping near the surface could affect the wave propagation—by generating meridional convergence into the surface low ahead of the heating, as seen in Fig. 7c. The GCM's heating is not in phase with the moisture convergence, but lags behind by about 40° of longitude (or three days); if one uses a more complete model in which this frictional convergence is present, a standard CISK formulation would be inadequate for modeling the heating.

Solutions of this set of equations are sought with the longitude–time dependence $\exp[ik(x - ct)]$, and the resulting eigenvalue equation is solved for the complex phase speed c. These phase speeds are independent of the zonal wavenumber k. Given the model's finite-differencing, eight vertical modes are obtained. All of these modes are neutral if r_0 is smaller than 7×10^{-3}. The eigenvalue calculation yields an instability for $r_0 > 7 \times 10^{-3}$. Only one unstable mode exists throughout the range of realistic r_0. The complex phase speed of the unstable mode is shown in Fig. 17 as a function of r_0. Also shown are the neutral modes from which the unstable mode emerges as r_0 increases. For the value $r_0 = 15 \times 10^{-3}$ typical of the equator in the GCM, the

phase speed of the model is 17 m s^{-1} and the e-folding time (kc_I) for zonal wavenumber 1 is eight days. The precise manner in which this mode evolves from the dry atmosphere's neutral modes as r_0 increases is of no physical significance, since these neutral modes are artifacts of the vertical discretization and upper boundary condition. The unstable mode does have physical significance since it decays away from the tropospheric source; it is essentially the most unstable CISK mode found originally by Hayashi (1970).

The structure of the zonal wind and temperature perturbations in the unstable mode for wavenumber 1 and $r_0 = 15 \times 10^{-3}$ is shown in Fig. 18. The phase is chosen so that the heating generated by the wave is centered at λ_0, and the amplitude is chosen so that the maximum zonal wind perturbation at low levels equals 5 m s^{-1}, as in the GCM composite (Fig. 10). (In comparing the figures, one should keep in mind that Fig. 18 consists of wavenumber 1 only, while the composites in Figs. 10 and 11 are mostly a mix of wavenumbers 1 and 2.) This CISK mode exhibits the same westward tilt with height as the disturbance in the GCM composites (Figs. 10 and 11) and the linear response (Fig. 14). The temperatures are in quadrature with the heating in the lower troposphere and in phase in the upper troposphere, as in Fig. 10, but the temperature perturbations are too large, particularly in the lower troposphere. The phase shift between the upper- and lower-tropospheric divergence seen in Fig. 18 is not shared
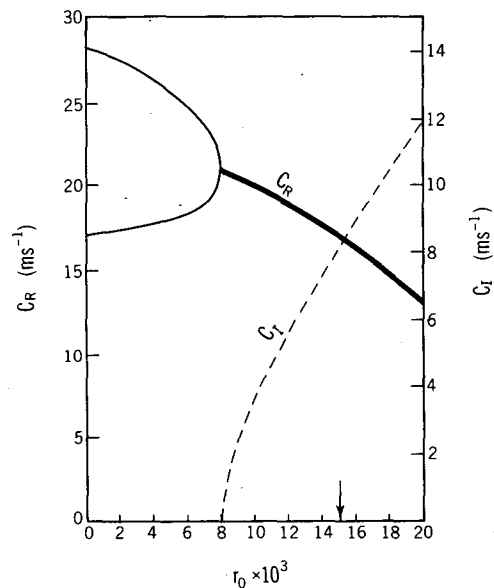

FIG. 17. The real c_R (solid curves) and imaginary c_I (dotted curve) parts of the complex phase speed obtained from the wave-CISK model, as functions of the low-level water-vapor mixing ratio, r_0. Only those two neutral modes from which the one unstable mode emerges are shown. The value $r_0 = 15 \times 10^{-3}$ typical of the GCM atmosphere at low levels over the equator is highlighted by an arrow.
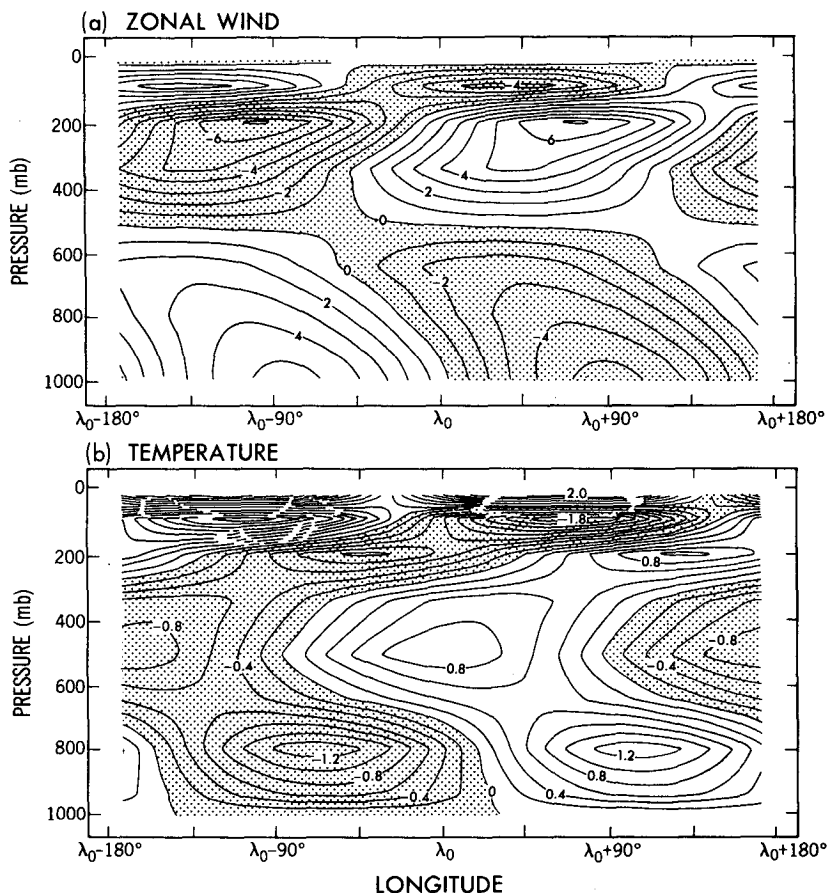
FIG. 18. Longitude–pressure distributions of (a) zonal wind (contour interval: 1 m s^{-1}) and (b) temperature (contour interval: 0.2°C), as obtained from the solution of the wave-CISK model with $r_0 = 15 \times 10^{-3}$. The center of the heating is located at the reference longitude in the middle of the x-axis.

by the GCM composite, however. Some discrepancies are to be expected in any case, since the composite describes the mature finite amplitude disturbance and not an amplifying wave. We have not attempted to construct a composite of the amplifying stage, since the period of amplification is so vague in Fig. 4.

This analysis does not explain why the wavenumber 1 and 2 Kelvin waves should dominate the zonal velocity spectra, as opposed to smaller scale Kelvin waves or disturbances with other meridional structures. In particular, this instability yields c_i independent of k and, therefore, largest growth rates (kc_i) at the smallest scales. One must assume that the nonlinear equilibration somehow favors the largest scale Kelvin modes.

The phase speed of the unstable mode can be reduced by lowering the center of mass of the heating, as is most simply seen in the three-layer model discussed by Takahashi (1987). For example, the heating profile defined by the dotted lines in Fig. 16 produces an unstable wave with a phase speed of 10 m s^{-1}, close to that in the observations, when $r_0 = 15 \times 10^{-3}$. Since

this modified heating profile appears to be even less realistic than the GCM's, it is difficult to argue that the GCM's propagation speed is too fast because its heating is too deep.

7. Conclusions

This paper describes the structure of the tropical intraseasonal oscillations of an idealized GCM with a zonally symmetric climate and fixed surface temperatures. The model has a well-defined spectral peak in velocity potential and zonal wind for eastward-moving wavenumber 1 at a period of about 25 days, which we associate with the Madden–Julian oscillation, despite the difference in frequency. Wavenumber 2 has a spectral peak at a similar phase speed (≈ 18 m s^{-1}). However, the individual small-scale disturbances in which the model's precipitation is organized do not propagate steadily at this phase speed, unlike the models of Hayashi and Sumi (1986) or Swinbank et al. (1988). Instead, the 18 m s^{-1} speed characterizes the downstream

redevelopment of new disturbances. This difference between the models is most likely due to differences in convective parameterization schemes.

A composite of the GCM oscillation is constructed that focuses on the larger scales. At upper-tropospheric levels, the structure is suggestive of a Kelvin wave in that meridional velocities are small. The anticyclone pair observed to be associated with the heating (e.g., Knutson and Weickmann 1987, Figs. 13 and 14) is present only faintly. When we modify our filter to accept lower frequencies, below the spectral peak, these anticyclones are strengthened. Hence, it is likely that the observed anticyclones are associated with fluctuations on time scales that are longer than those considered here. The structure of the composite also differs from a simple Kelvin wave at upper levels in that the geopotential amplitude peaks at a higher level than the zonal flow.

An interesting aspect of the low-level flow is that the convergence lies east of the center of heating by about 30° longitude. As a result, the low-level moisture convergence peaks at a given point about three days before the peak in precipitation. It seems plausible that this shift should favor eastward-propagating disturbances. Positive moisture anomalies are also found ahead of the disturbance in the boundary layer, but it would take much less than three days to create these anomalies, given the amplitude of the moisture convergence.

Positive evaporation anomalies are created east of the heating by the superposition of perturbation easterlies and the mean easterlies. These evaporation anomalies are important for the amplitude of the oscillation, as demonstrated by NHC. That they do not determine the characteristic phase speed of the oscillation is clear from the swamp model results in NHC. In that model, the removal of the wind speed dependence of the evaporation has little effect on the oscillation. Composites for the swamp model show a very similar three-dimensional structure to that described here, except that the amplitudes of the zonal wind perturbations near the surface are smaller.

Given the three-dimensional structure of the heating and the phase speed, a linear steady wave model is found to give a rough approximation to the flow and temperature structures in the GCM composite, as long as one adds strong damping both near the surface and above the heated region. The damping above the heating is needed to dissipate the upward-propagating waves with short vertical wavelength excited by the source. How these waves are dissipated in the GCM is unclear; they are severely distorted by the crude vertical resolution of the model in any case.

A simple Kelvin-wave CISK model, with the vertical structure of the heating (as well as background temperature and moisture profiles) based on the GCM composite, yields one and only one unstable mode. This mode has a phase speed in good agreement with that simulated in the GCM. The success of this model

is surprising, particularly since it ignores the substantial phase shift between the low-level moisture convergence and the precipitation seen in the GCM composite. The phase speed of this unstable mode can be lowered to that of the observations (≈ 10 m s^{-1}) by lowering the center of mass of the heating. But this explanation for the GCM's distortion of the phase speed is unpalatable, since one usually thinks of a convective adjustment scheme (as opposed to a scheme with explicit penetrative convection) as underestimating, not overestimating, the height of this center of mass. One must consider the possibility that the CISK mechanism is less important for phase speed selection in the atmosphere than in the model.

APPENDIX A

The Climatological Precipitation

Figure A1 shows the time–mean precipitation as a function of latitude in the GCM. There is no hint of an equatorial minimum in the precipitation. This is distinctly different from the models of Hayashi and Sumi (1986) and Swinbank et al. (1988), both of which have well-defined equatorial dry zones. While the model we analyze here has coarser horizontal resolution
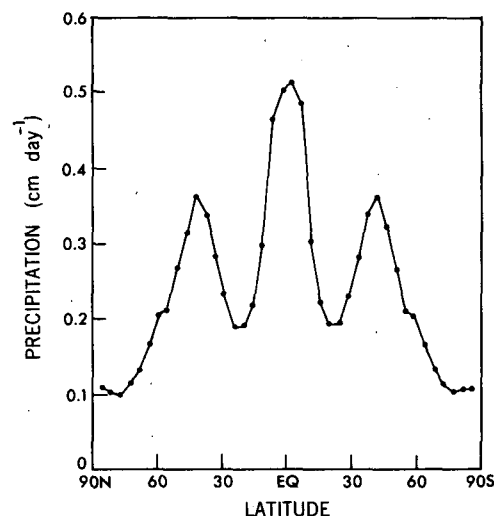

FIG. A1. Variation with latitude of the temporally and zonally averaged precipitation rate for the idealized GCM used in this study.

than either of these other idealized GCMs, and a different convective parameterization, we suspect that these are not responsible for this difference. We think that the difference results from the choice of surface temperatures.

We have set the fixed surface temperatures in our model to the values predicted by the companion swamp model, in which a condition of zero energy flux through the lower boundary is enforced. Since there is net radiative heating of the atmosphere at the equator, and since there is no heat flux through the lower boundary in the swamp model and, therefore, no implied oceanic heat transport, we expect the swamp model atmosphere to transport energy poleward. Assuming that the transfer of sensible, latent and geopotential energy by the mean meridional circulation balances the radiative heating in the tropics, a pair of Hadley circulation cells must straddle the equator, with ascent over the deep tropics. Now consider a fixed SST model with the same surface temperature as the swamp model. The dynamics of the two models should be very similar, so the heat fluxes through the lower boundary should also be very small. Thus, the energetics argument outlined above should also hold for the fixed SST model, and we likewise expect rising motion over the equator. This suggests that if Hayashi and Sumi and Swinbank et al. had performed a swamp calculation and used the mean temperature so produced as boundary conditions for the fixed surface temperature model, then their climatology would have been similar to ours.

APPENDIX B

CISK Finite-Differencing

The GCM's temperature, geopotential, and horizontal velocity are defined at the full σ-levels, $\{\sigma_k, k = 1, 9\}$, listed in Table B1. The vertical velocity ω is defined on half σ-levels with $\omega = 0$ at $\sigma_{1/2}$ and $\sigma_{9+1/2}$ and $\sigma_k = (\sigma_{k+1/2} + \sigma_{k-1/2})/2$. The model's hydrostatic equation is

$$\Phi_{k+1} - \Phi_k = -T_{k+1}\,\xi^+_{k+1/2} - T_k\xi^-_{k+1/2}, \quad \text{(B1)}$$

where

$$\xi^+_{k+1/2} = R\ln(\sigma_{k+1}/\sigma_{k+1/2}),$$

$$\xi^-_{k+1/2} = R\ln(\sigma_{k+1/2}/\sigma_k).$$

For a disturbance with phase speed c and wavenumber k, the model's continuity equation and zonal equation of motion reduce to

$$c(W_{k+1/2} - W_{k-1/2})/\Delta_k = -ik\Phi_k, \quad \text{(B2)}$$

where

$$\Delta_k \equiv \sigma_{k+1/2} - \sigma_{k-1/2},$$

and $W \equiv \omega/p_*$. The corresponding thermodynamic equation reads

TABLE B1. The pressure levels $\sigma_k = p_k/p_*$ ($p_* = 1$ bar), mean atmospheric temperature profile $\bar{T}_k$, and heating profile f_k, used in the CISK calculation.

k	σ_k	$\bar{T}_k$	f_k
1	0.025	240.0	0
2	0.095	190.9	0
3	0.205	218.2	0.57
4	0.350	244.1	1.46
5	0.515	264.7	2.12
6	0.680	278.4	1.79
7	0.830	287.5	0.32
8	0.940	294.2	0
9	0.990	298.4	0

$$ikcT_k = W_{k+1/2}S_k^+ + W_{k-1/2}S_k^- - Q_0f_k/c_p, \quad \text{(B3)}$$

where

$$S_k^+ = (\bar{T}_{k+1/2} - \bar{T}_k)/(\sigma_{k+1/2} - \sigma_k) - \kappa\bar{T}_k/\sigma_k,$$

$$S_k^- = (\bar{T}_k - \bar{T}_{k-1/2})/(\sigma_k - \sigma_{k-1/2}) - \kappa\bar{T}_k/\sigma_k,$$

$$\sum_{k=1}^{9} f_k\Delta_k = 1, \quad \text{and} \quad Q_0 = \sum_{k=1}^{9} r_k(W_{k-1/2} - W_{k+1/2}).$$

The vertical structure of the heating, f_k, and the basic state temperature profile, $\bar{T}_k$, are listed in Table B1. The mixing ratio r_k is set equal to r_0R_k, where $R_8 = R_9 = 1$, $R_7 = 0.5$, and $R_k = 0$ for $k < 7$.

The three sets of equations, (B1), (B2) and (B3), are easily combined into one set of equations for the vertical velocity. Using the boundary conditions $W_{1/2} = W_{9+1/2} = 0$, the result is a matrix eigenvalue problem of the form

$$c^2\mathbf{A}W = \mathbf{B}W, \quad \text{(B4)}$$

where $\mathbf{A}$ and $\mathbf{B}$ are 8×8 matrices.

REFERENCES

Emanuel, K. A., 1987: An air–sea interaction model of intraseasonal oscillations in the tropics. *J. Atmos. Sci.*, **44**, 2324–2340.

Garcia, R. R., and M. L. Salby, 1987: Transient response to localized episodic heating in the tropics. Part II: Far field behavior. *J. Atmos. Sci.*, **44**, 499–530.

Hayashi, Y., 1970: A theory of large-scale equatorial waves generated by condensation heat and accelerating the zonal wind. *J. Meteor. Soc. Japan*, **48**, 140–160.

——, and D. G. Golder, 1986: Tropical intraseasonal oscillations appearing in a GFDL general circulation model and FGGE data. Part I: Phase propagation. *J. Atmos. Sci.*, **43**, 3058–3067.

——, and S. Miyahara, 1987: A three-dimensional linear response model of the tropical intraseasonal oscillation. *J. Meteor. Soc. Japan*, **65**, 843–852.

Hayashi, Y.-Y., and A. Sumi, 1986: The 20–40 day oscillation simulated in an "aqua-planet" model. *J. Meteor. Soc. Japan*, **64**, 451–466.

Hendon, H. H., 1988: A simple model of the 40–50 day oscillation. *J. Atmos. Sci.*, **45**, 569–584.

Knutson, T. R., and K. M. Weickmann, 1987: 30–60 day atmospheric

oscillations: Composite life cycles of convection and circulation anomalies. *Mon. Wea. Rev.,* **115,** 1407–1436.

Lau, K.-M., and T. J. Phillips, 1986: Coherent fluctuations of extratropical geopotential height and tropical convection in intraseasonal time scales. *J. Atmos. Sci.,* **43,** 1164–1181.

——, and L. Peng, 1987: Origin of low-frequency (intraseasonal) oscillations in the tropical atmosphere. Part I: Basic theory. *J. Atmos. Sci.,* **44,** 950–972.

Lau, N.-C., and K.-M. Lau, 1986: The structure and propagation of intraseasonal oscillations appearing in a GFDL general circulation model. *J. Atmos. Sci.,* **43,** 2023–2047.

Lorenc, A. C., 1984: The evolution of planetary-scale 200 mb divergent flow during the FGGE year. *Quart. J. Roy. Meteor. Soc.,* **110,** 427–441.

Madden, R. A., 1987: Relationships between changes in the length-of-day and the 40–50 day oscillation in the tropics. *J. Geophys. Res.,* **92,** 8391–8399.

——, and P. R. Julian, 1971: Detection of a 40–50 day oscillation in the zonal wind in the tropical Pacific. *J. Atmos. Sci.,* **28,** 702–708.

——, and ——, 1972: Description of global-scale circulation cells in the tropics with a 40–50 day period. *J. Atmos. Sci.,* **29,** 1109–1123.

Manabe, S., J. Smagorinsky and R. F. Strickler, 1965: Simulated climatology of a general circulation model with a hydrologic cycle. *Mon. Wea. Rev.,* **93,** 769–798.

Miyahara, S., 1987: A simple model of the tropical intraseasonal oscillation. *J. Meteor. Soc. Japan,* **65,** 341–351.

Murakami, T., and T. Nakazawa, 1985: Tropical 45 day oscillations during the 1979 Northern Hemisphere summer. *J. Atmos. Sci.,* **42,** 1107–1122.

Neelin, J. D., I. M. Held and K. H. Cook, 1987: Evaporation–wind feedback and low-frequency variability in the tropical atmosphere. *J. Atmos. Sci.,* **44,** 2341–2348.

Nigam, S., I. M. Held and S. W. Lyons, 1986: Linear simulation of the stationary eddies in a general circulation model. Part I: The no-mountain model. *J. Atmos. Sci.,* **43,** 2944–2961.

Swinbank, R., T. N. Palmer and M. K. Davey, 1988: Numerical simulations of the Madden and Julian oscillations. *J. Atmos. Sci.,* **45,** 774–788.

Takahashi, M., 1987: A theory of the slow phase speed of the intraseasonal oscillation using the wave-CISK. *J. Meteor. Soc. Japan,* **65,** 43–49.

Wang, B., 1988: The dynamics of tropical low-frequency waves: An analysis of the moist Kelvin wave. *J. Atmos. Sci.,* **45,** 2051–2065.